

# 1 Local density determines nuclear movements during 2 syncytial blastoderm formation in a cricket

## 3 *Supplemental Information*

4 Seth Donoughe<sup>1,2,\*</sup>, Jordan Hoffmann<sup>3</sup>, Taro Nakamura<sup>1,4</sup>, Chris H. Rycroft<sup>3,5,\*</sup>, Cassandra G. Extavour<sup>1,6,\*</sup>  
5

## 6 Contents

7	<b>1 Processing, segmenting, and tracking microscopy datasets</b>	<b>2</b>
8	1.1 Datasets from lightsheet microscopy . . . . .	2
9	1.2 Datasets from epifluorescence microscopy . . . . .	2
10	1.3 Datasets from confocal microscopy . . . . .	3
11	1.4 Uses of each type of microscopy data . . . . .	3
12	1.5 Accuracy of automated nucleus tracking . . . . .	4
13	<b>2 Quantitative measurements of nucleus behavior</b>	<b>4</b>
14	2.1 Nucleus speed . . . . .	4
15	2.2 Correlation of nucleus movement vectors . . . . .	5
16	2.3 Local nucleus density . . . . .	5
17	2.4 Rate of change in number of nuclei . . . . .	6
18	2.5 Motion toward open space . . . . .	6
19	<b>3 Supplemental movie of yolk and nucleus movements</b>	<b>6</b>
20	<b>4 Simulating blastoderm formation</b>	<b>7</b>
21	4.1 Overview and aim . . . . .	7
22	4.2 Model components . . . . .	7
23	4.2.1 Embryo . . . . .	8
24	4.2.2 Division geometry . . . . .	8
25	4.2.3 Density-dependent cell cycle duration . . . . .	8
26	4.2.4 Asymmetric pulling cloud . . . . .	8
27	4.2.5 Bias of nucleus movement toward periplasm . . . . .	9
28	4.3 Assessing a model of mutual repulsion . . . . .	10
29	<b>5 Methods for physically constricting embryos</b>	<b>10</b>
30	5.1 Assembling the embryo constriction device . . . . .	10
31	5.2 Using the embryo constriction device . . . . .	10

\*Corresponding authors. E-mail: [donoughe@uchicago.edu](mailto:donoughe@uchicago.edu), [chr@seas.harvard.edu](mailto:chr@seas.harvard.edu), [extavour@oeb.harvard.edu](mailto:extavour@oeb.harvard.edu)

<sup>1</sup>Department of Organismic and Evolutionary Biology, Harvard University, Cambridge, MA, USA

<sup>2</sup>*Present address:* Department of Molecular Genetics and Cell Biology, University of Chicago, Chicago, IL, USA

<sup>3</sup>John A. Paulson School of Engineering and Applied Sciences, Harvard University, Cambridge, MA, USA

<sup>4</sup>*Present address:* Division of Evolutionary Development, National Institute for Basic Biology, Okazaki, Japan

<sup>5</sup>Computational Research Division, Lawrence Berkeley Laboratory, Berkeley, CA, USA

<sup>6</sup>Department of Molecular and Cellular Biology, Harvard University, Cambridge, MA, USA

32	<b>6 Code, data, and materials availability</b>	<b>13</b>
33	<b>References</b>	<b>13</b>

## 34 **1 Processing, segmenting, and tracking microscopy datasets**

35 The *Methods* section of the main text includes information on animal culture, collecting embryos, mounting sam-  
36 ples, and microscope settings. This section contains details on how we processed datasets for analysis.

### 37 **1.1 Datasets from lightsheet microscopy**

38 We fused multiview lightsheet datasets with the Multiview Reconstruction plugin<sup>1,2</sup> for Fiji<sup>3,4</sup> (version 2.0.0-rc-30  
39 through 2.1.0/1.5.3). Fluorescent beads (ThermoFisher F8821) embedded in the agarose served as fiducial markers  
40 for registration; we used them to align and combine multiple views as a weighted average fusion<sup>1</sup>. We deconvolved  
41 datasets for ten iterations with the Multiview Reconstruction plugin<sup>2</sup> on a 32-core workstation with 128 GB of  
42 RAM running Ubuntu 14.04.

43 We performed nucleus segmentation and automated tracking with Ilastik<sup>5</sup> (versions 1.1.5 to 1.3.0). We imported all  
44 data as a 4D sequence, manually trained a pixel classifier to differentiate nuclei from background, and identified  
45 nuclei using the object classification tool. Then we used Ilastik's automated tracking tool to track all nucleus move-  
46 ments. We used a custom Mathematica script to convert the automated tracking output from Ilastik into an XML  
47 file that was parsable by MaMuT<sup>6</sup>, the semi-automated tracking plug-in for Fiji<sup>3</sup>. The script to generate the XML  
48 file, as well as those needed run the simulations in this study, are available on the GitHub repository that accom-  
49 panies this paper ([https://github.com/hoffmannjordan/gryllus\\_nuclear\\_movements](https://github.com/hoffmannjordan/gryllus_nuclear_movements)). Note: the  
50 ability to directly transfer object tracks from Ilastik to MaMuT is now included in Ilastik (version 1.3.3). Last, we  
51 used MaMuT to manually identify each division and stitch together the Ilastik-generated tracks, which resulted in  
52 continuously tracked lineages. For embryos mounted in this manner, approximately two-thirds of the radial depth  
53 of the embryo could be imaged clearly (as measured from the surface to a center line connecting the anterior and  
54 posterior poles of the embryo), while the signal from the inner-most portion of the embryo was diffused by the  
55 yolk of the embryo.

### 56 **1.2 Datasets from epifluorescence microscopy**

57 We recorded multiple embryos at a time by tiling across a field of microwells, each of which held a single embryo,  
58 oriented laterally, following previously described methods<sup>7</sup>. We used Ilastik to automatically track nucleus move-  
59 ments and manually identified division in MaMuT. For embryos mounted in this manner, approximately one-half  
60 to one-third of the  $z$ -depth of the embryo could be imaged clearly, while the signal from the rest of the embryo was  
61 diffused by the yolk of the embryo. Thus, the number of well-segmented nuclei fluctuated slightly between time  
62 points, depending on the particular paths traveled by individual nuclei; the effect of this variability was strongest for

63 the first few division cycles. Therefore, for two-dimensional timelapse (2D+T) datasets, we performed automated  
64 analysis on these datasets beginning at the earliest time point when there were at least 25 nuclei.

### 65 **1.3 Datasets from confocal microscopy**

66 We included three-dimensional timelapse (3D+T) datasets of embryos laid by females with Act-mtdT and Act-  
67 H2B-EGFP transgenes<sup>8</sup>. We used a magnification such that approximately one-fifth of the length and one-half of  
68 the breadth of an embryo was recorded at a time. We cropped and assembled these into figures using Fiji. Details  
69 of the genotypes of these transgenic lines are included in the main text Methods section *Transgenics and animal*  
70 *culture*.

### 71 **1.4 Uses of each type of microscopy data**

72 *Multiview lightsheet datasets of blastoderm formation:* These 3D+T datasets enabled us to reconstruct nucleus  
73 movements and divisions in detail. We recorded these datasets one at a time. After a syncytial blastoderm had  
74 formed, we removed the embryo from its agarose column and cultured it in an incubator as described in the main  
75 text Methods section *Collecting and culturing embryos*. Once the embryo hatched, we continued with processing  
76 and tracking the nuclei. We tracked and processed four such 3D+T datasets. Figures 1B, 1D, 2A-E, and 3A-H in the  
77 main text show data from a single such embryo (the same embryo in all cases). We followed the same procedures and  
78 repeated the same analyses on three additional lightsheet datasets. In all cases we found the same patterns shown  
79 in Figures 1, 2, and 3: a positive association between cycle duration and nuclear density, biphasic speeds within each  
80 cell cycle, a negative association between speed and density in Phase A, and a tendency for Phase A nuclei to move  
81 into nearby open space when they are in the interior of the embryo (data not shown).

82 *Epifluorescence datasets of blastoderm formation:* We also recorded 60 additional 2D+T datasets. Three of these  
83 datasets are included in Fig. 5 in the main text as unmanipulated controls to compare to the physically constricted  
84 embryos.

85 *Epifluorescence datasets of constricted embryos:* We recorded 2D+T datasets of physically constricted embryos, im-  
86 aged using epifluorescence. These data are shown in Fig. 5 of the main text. In our hands, constricted embryos  
87 did not hatch, and instead they arrested partway through development (in some cases before a blastoderm had  
88 formed, and in others afterwards). The furthest extent of development we observed was just before katrepsis  
89 occurred<sup>9</sup>. Our criteria for including a constriction dataset in the data analysis were as follows: no visible ruptures  
90 of the eggshell, no cessation of nucleus movements before the syncytial blastoderm was formed, and no nuclear ag-  
91 gregations during the developmental period under study. In our recordings of unmanipulated embryos, we found  
92 that these criteria reliably predicted that blastoderm formation and subsequent development would proceed. We  
93 analyzed three constricted embryos that satisfied the criteria for inclusion (see Fig. 5 of the main text).

94 *Confocal datasets of yolk and nucleus movement:* We used these datasets to qualitatively assess the movements of  
95 yolk and nuclei. The results are shown in Fig. 1 of the main text and in Supplemental File 2.

## 96 1.5 Accuracy of automated nucleus tracking

97 To assess the accuracy of automated nucleus tracking for lightsheet datasets, we manually tracked a set of nuclei  
 98 from an embryo and compared the nucleus positions to the output from automated tracking on the same dataset.  
 99 Specifically, we took the first 300 successive frames and applied the semi-automated tracking tool in MaMuT<sup>6</sup>.  
 100 Next, we inspected each nucleus position and tracking link, and manually corrected any incorrect positions or links,  
 101 resulting in 41,092 single time-point nucleus observations. Then, we used Ilastik to segment and automatically track  
 102 the same dataset.

103 Treating the manually-corrected dataset as ground truth, we assessed the accuracy of the automated approach by  
 104 calculating the distance from each nucleus in the manually-corrected dataset to the closest corresponding nucleus  
 105 in the automatically-tracked dataset. Table 1 shows percentiles of these distances.

<i>Percentile</i>	<i>Distance (<math>\mu\text{m}</math>)</i>
10%	0.6
25%	0.9
50%	1.4
75%	1.9
90%	2.9

Table 1: **Tracking discrepancy.** Percentiles of spatial discrepancies between each nucleus in a manually tracked dataset and the closest corresponding nucleus in an automatically tracked dataset. We calculated distances for 41,092 manually tracked nucleus-time points.

## 106 2 Quantitative measurements of nucleus behavior

### 107 2.1 Nucleus speed

108 For 3D+T datasets, we defined a vector

$$\vec{x}_t = (x_t, y_t, z_t) \quad (1)$$

109 for a nucleus position at time  $t$ . Using this notation, we defined instantaneous nucleus speed,  $s_t$ , as half of the  
 110 displacement over two time points,

$$s_t = \frac{1}{2} \|\vec{x}_{t+2} - \vec{x}_t\|. \quad (2)$$

111 For 2D+T datasets, we defined speed in an analogous manner, calculating movement only in the  $xy$  plane. The  
 112  $z$ -component of motion was not available in such datasets, which meant that calculated speeds are an underestimate  
 113 of the true nucleus speed in 3D space.

## 114 2.2 Correlation of nucleus movement vectors

115 For each embryo, we re-oriented the set of  $\vec{x}_t$  across all  $t$  so that the first principal component lay along the  $x$  axis,  
 116 in effect rotating the dataset so that the long axis of the embryo was parallel to the  $x$  axis. By convention, we also  
 117 oriented each embryo with the posterior end pointed toward the positive  $x$  direction. For each  $\vec{x}_t$ , we computed  
 118 the motion vector from  $\vec{x}_t$  to  $\vec{x}_{t+2}$ , and then used it to calculate the correlation between pairs of nuclei moving at  
 119 the same time (results shown in Fig. 1D of the main text).

## 120 2.3 Local nucleus density

121 We defined local nucleus density around a given focal nucleus as the number of other nuclei within radius  $\mathcal{R} =$   
 122  $150 \mu\text{m}$ .<sup>†</sup> For a nucleus near the periplasm of the embryo, the sphere of space within  $\mathcal{R}$  included some volume  
 123 that was outside of the embryo itself, but we did not wish to include this space when calculating local nucleus  
 124 density. Therefore, we needed to numerically represent the surface of the eggshell so that we could exclude the  
 125 volume external to the embryo from consideration in calculating local density. We took a single time point at  
 126 the uniform blastoderm stage that was imaged with a multiview lightsheet microscope, segmented the nuclei, and  
 127 fitted a parabola to the anterior-posterior (A-P) axis of the cloud of points. We used this parabola to transform the  
 128 positions of nuclei by mapping the parabola to a straight line. Then we calculated the convex hull of the transformed  
 129 points, and applied the reverse transformation to the convex hull. This produced the volume  $\mathcal{B}$ .

130 We took the sphere  $\mathcal{S}$  defined by  $\mathcal{R}$ , and then defined

$$V = \text{volume}(\mathcal{S} \cap \mathcal{B}). \quad (3)$$

131 The volume fraction was computed as

$$\phi = \frac{V}{\frac{4}{3}\pi\mathcal{R}^3} \quad (4)$$

132 and the local density was defined as

$$\rho = \frac{\#}{\phi}, \quad (5)$$

133 where  $\#$  represents the count of nuclei within  $\mathcal{R}$ .

134 For 2D+T datasets, local nucleus density was treated in an analogous manner: we computed the region of overlap  
 135 of a  $150 \mu\text{m}$  circle with the 2D convex hull of all nuclei at the blastoderm stage. Then we counted the number of  
 136 nuclei within that area and calculated the area-weighted density as above. This meant that nuclear densities were

<sup>†</sup>We found that when we defined *local nucleus density* as the the number of other nuclei within  $\mathcal{R} = 150 \mu\text{m}$ , across the range of densities found during cricket blastoderm formation, we observed a positive association between local nucleus density and mitotic cycle duration (main text Fig. 2C-E). Similarly, we observed a negative association between local nucleus density and nucleus speed (main text Figure 3E). We found that these results were not sensitive to the exact  $\mathcal{R}$  we that chose. The same associations were obtained for radii from 50 to 300  $\mu\text{m}$  (data not shown).

137 calculated from volumes with different shapes in the 3D+T vs. 2D+T datasets (i.e. spherical vs. cylindrical), and  
 138 therefore their measured values cannot be compared to one another in absolute terms. Instead, we consider it  
 139 appropriate to compare density-dependent results between datasets that were imaged in the same manner.

## 140 2.4 Rate of change in number of nuclei

141 Early in cricket embryogenesis, we could not rule out the possibility that some nuclei passed through the middle of  
 142 the embryo (see I.1), where their observable fluorescence signal was sufficiently diffuse that we could not detect and  
 143 track the nuclei at all. Therefore, rather than counting nuclei directly at each time point, we used *percent change in*  
 144 *nucleus number* as a proxy for nucleus division. Because the number of detected nuclei fluctuated slightly from one  
 145 time point to the next, we smoothed the total number of nuclei present by applying a Gaussian blur with a width  
 146 of three time points. Using Mathematica, an interpolant,  $N(t)$ , was fit through the data. We differentiated this  
 147 function to produce  $N'(t)$ . To estimate a rate of change in the number of nuclei over time, we divided  $N'(t)/N(t)$ .  
 148 As a result, percent change was briefly calculated to be negative in the first few division cycles.

## 149 2.5 Motion toward open space

150 We defined direction towards the “largest open space” as the vector oriented towards the centroid of the 3D Voronoi  
 151 cell formed by each nucleus, bounded by the inner surface of the eggshell, as approximated by the convex hull of  
 152 nuclei at the blastoderm stage.

153 For each nucleus, we considered  $\vec{v} = \frac{1}{2} (\vec{x}_{t+2} - \vec{x}_t)$ , and calculated its correlation  $c$  with a vector into the direction  
 154 into open space,  $\vec{s}$ , as

$$c = \frac{\vec{x} \cdot \vec{s}}{\|\vec{x}\| \|\vec{s}\|}. \quad (6)$$

155 To account for timepoint-to-timepoint noise in this calculation, we calculated average “movement into space” vec-  
 156 tors for each nucleus over a sliding window of three time points. In addition, we computed the shortest distance  
 157 from all nucleus locations  $\vec{x}_t$  to the inner surface of the eggshell,  $d_S$ . We binned nuclei by  $d_S$  into those that were  
 158 near the surface ( $d_S < 75 \mu\text{m}$ ) and those that were far from the surface ( $d_S \geq 75 \mu\text{m}$ ), as shown in main text  
 159 Fig. 3G,H.

## 160 3 Supplemental movie of yolk and nucleus movements

161 We have included an example movie as Supplemental File 2. This dataset was captured as follows:

- 162 • *Genotype:* Act-H2B-EGFP; Act-mtdT
- 163 • *Subject:* The field of view was centered 20% of the way from the anterior pole of the embryo, captured during  
 164 the period of syncytial development when nuclei were initially reaching the anterior pole of the embryo.

- 165 • *Z-step*: 2.5 microns
- 166 • *Duration*: 132 time steps
- 167 • *Time interval*: 2 minutes
- 168 • *xy resolution*: 1 pixel = 0.327  $\mu\text{m}$
- 169 • *Image processing*: 17 consecutive z-slices were combined with as a maximal intensity projection (MIP). In  
170 order to image a given nucleus and its surrounding yolk, we only needed two to three z-slices of this thickness.  
171 We used more z-slices to capture more nuclei in a single video.

172 This movie illustrates that there are no obvious bulk flows of yolk, either during the phase when nuclei are moving  
173 (“Phase A”) or when they are relatively immobile (“Phase B”).

## 174 4 Simulating blastoderm formation

### 175 4.1 Overview and aim

176 As described in the main text, the goal of our modeling approach was to assess whether a local, asymmetric, active  
177 pulling force on each nucleus could satisfactorily recapitulate the empirical patterns of nucleus behaviors. Here we  
178 report on the model in closer detail. The simulation is performed in a  $202 \times 92 \times 92$  volume region. We verified  
179 results are consistent with scaling up the grid by a factor of two, but for time efficiency we opted to use the smaller  
180 grid. The simulation time step is  $T = 45$  s corresponding to half a time step from the lightsheet data. The embryo  
181 used for the fit of the simulation boundary was 2421  $\mu\text{m}$  long, and thus the grid spacing is  $L = 11.98$   $\mu\text{m}$ .

### 182 4.2 Model components

183 We simulated the center of each nucleus  $\vec{x}_i(t)$  as a function of time. The nucleus positions followed the differential  
184 equation

$$\alpha M \frac{d^2 \vec{x}_i}{dt^2} + \gamma \left( \frac{d\vec{x}_i}{dt} - \vec{v}^{cyt}(\vec{x}_i(t)) \right) = \vec{F}_i^{tot} \quad (7)$$

185 where  $M$  is an arbitrary mass scale and  $\alpha M$  is the mass of a nucleus,  $\gamma$  is a drag coefficient between the nucleus  
186 and the cytoplasm, and  $\vec{F}_i^{tot}$  is the sum total of forces on the nucleus. Based on our experimental results, we as-  
187 sumed that  $\vec{v}^{cyt} = \vec{0}$  and we did not simulate any viscous or viscoelastic flow in the cytoplasm. We worked in the  
188 overdamped limit where the acceleration could be neglected, yielding

$$\frac{d\vec{x}_i}{dt} = \frac{1}{\gamma} \vec{F}_i^{tot}, \quad (8)$$

189 We simulated equation (8) using the first-order forward Euler method. We describe the different contributions to  
190 the force below. We take  $\gamma = 1M/T = 0.022M \text{ s}^{-1}$ .

#### 191 4.2.1 Embryo

192 We used the shape of a real cricket embryo, determined from the positions of nuclei during the uniform blastoderm  
193 stage, as described in Section 2.3. We approximated each cross section along the A-P axis  $z$  with an ellipse with radii  
194  $r_1(z)$  and  $r_2(z)$  with a center at  $(x(z), y(z))$ . This defined a boundary  $\mathcal{B}$ . For simulated *G. bimaculatus* embryos,  
195 we performed all calculations on the discretized 3D grid. The grid was used by the scikit-fmm library, which we used  
196 to compute the clouds for each nucleus.

#### 197 4.2.2 Division geometry

198 Nuclei divided in random directions (i.e. with random spindle orientation) throughout the simulation, irrespective  
199 of the proximity of neighbors, the proximity of the eggshell, or the orientation of previous divisions in a lineage.  
200 Newly divided daughter nuclei were created at  $\vec{x}^{mother} \pm \vec{n}(1 \mu\text{m})$ , where  $\vec{n}$  is a random unit normal. If this dis-  
201 placement resulted in a daughter nucleus landing outside the boundary of the embryo, we assigned a new position  
202 for the nucleus by projecting it back to the surface of the embryo boundary by finding the closest point on the  
203 surface.

#### 204 4.2.3 Density-dependent cell cycle duration

205 In the empirical data, we observed a strong positive association between local nucleus density and cell cycle duration  
206 (see Fig. 2 in the main text). We incorporated this relationship into our simulation directly. We fitted a logistic curve  
207 to the empirical density vs. cell cycle duration data (shown in Fig. 2 in the main text), and then drew from it with  
208 normally distributed noise, based on the density at nucleus birth. In the real embryos, we observed that the variation  
209 in cycle duration increased as density increased (Fig. 2C-E), so we fitted the variance to a global clock used in the  
210 simulation,  $(90 \text{ s}) + (270 \text{ s})(t - T)/T$ , where  $T$  was the total simulation time.

#### 211 4.2.4 Asymmetric pulling cloud

212 We hypothesized that there was a local, asymmetric, active pulling force on each nucleus. We describe the biological  
213 inspiration for this model in the main text. Here we describe the implementation of the model.

214 Our force calculation models the nuclei as spheres with a  $7.2 \mu\text{m}$  diameter. We modeled the motion of a nucleus by  
215 ascribing a pulling cloud that emerges from a single origin on the surface of the nucleus. The cloud grows uniformly  
216 in all directions to a maximal radius,  $R_{\text{max}} = 150 \mu\text{m}$ , except for where its growth is impeded by the surface of the  
217 nucleus from which it originated, the surface of another cloud region, or the inner surface of the eggshell.

218 For each nucleus, we computed this cloud region by using the Python library scikit-fmm<sup>10</sup>. We used a fast marching  
219 method<sup>11</sup>, which is a computationally efficient way to identify all the voxels in the discretized grid that should be  
220 assigned to each nucleus. Specifically, we initialized the locations of nuclei to be zeroes of a field  $T(\vec{x})$ . We then  
221 solved the Eikonal equation

$$|\nabla T(\vec{x})| = 1, \quad (9)$$

where  $T(\vec{x})$  describes the minimum travel time from a nucleus to each position. The fast marching method works by scanning outward from the nuclei positions to fill in the values of the  $T(\vec{x})$  on the discretized grid. It also keeps track of which nucleus is closest to each point  $\vec{x}$ . This allows us to efficiently compute the region  $\mathcal{R}_i$  that is closest to each nucleus  $\vec{x}_i$ . From here, we define the pulling cloud region  $\mathcal{V}_i$  by removing space that is further away than  $R_{\max}$ , and space that is occluded by the steric effects from the nucleus (*i.e.* where a ray from the cloud origin to  $\vec{x}$  intersects the nucleus).

Each point in the cloud region creates a tug toward its position. Since our model is based on the assumption that this tug arises from a set of microtubules emanating from the cloud origin, we scale the tug by a factor of  $1/r^2$  to account for the microtubule density, where  $r$  is the distance to the nucleus center.<sup>2</sup> Hence, the total force created by the cloud is given by the integral

$$\vec{F}_i^{cloud} = \int_{\mathcal{V}_i} \beta \frac{\vec{y} - \vec{x}_i}{\|\vec{y} - \vec{x}_i\|_2^3} d\vec{y}. \quad (10)$$

The parameter  $\beta = 0.00521M/T^2 = 2.57 \times 10^{-6} M s^{-2}$  was fit from experimental data where we matched the maximum speed at the 4-nucleus stage. The integral in Eq. (10) is performed by summing over all voxels in  $\mathcal{V}_i$ .

#### 4.2.5 Bias of nucleus movement toward periplasm

In *G. bimaculatus* embryos, the first zygotic division tends to occur about ~60% of the way along the A-P axis, as measured from the anterior pole of the embryo. During the first few cell cycles, nuclei spread apart in space, with some of them moving through “open space” across the yolk-rich middle of the embryo, and others moving within the periplasm, close to the inner surface of the eggshell. The nuclei ultimately move into the periplasm and stay there (see Fig. 1A, B). Because nuclei travel varied paths and arrive in the periplasm asynchronously, we model their movement into the periplasm as a small bias that contributes additively to their movement. Specifically, for each nucleus  $\vec{x}_i$  we introduced a component to a nucleus’s motion vector that is in the direction of the nearest point  $\vec{y}_i$  on the inner surface of the eggshell. We define the vector  $\vec{q}_i = \vec{y}_i - \vec{x}_i$ . The contribution to the force is given by

$$\vec{F}_i^{surface} = \zeta \|\vec{F}_i^{cloud}\| \frac{\vec{q}_i}{\|\vec{q}_i\|} \quad (11)$$

where  $\zeta$  is a dimensionless constant. We include a factor  $\|\vec{F}_i^{cloud}\|$  since it is an existing force scale in the model. We used a value of  $\zeta = \frac{1}{3}$  to match the bias towards the periplasm in the empirical data.

<sup>2</sup>Technically it would be more consistent with the model to normalize by  $1/\tilde{r}^2$ , where  $\tilde{r}$  is the distance to the cloud origin on the nucleus surface. However, this could create numerical difficulties since the cloud origin is on the boundary of  $\mathcal{V}_i$  and thus  $\tilde{r}$  can become arbitrarily small. Since the cloud origin and nucleus center are close, using  $r$  instead of  $\tilde{r}$  has a minimal effect on the outcome and is more numerically stable.

### 245 4.3 Assessing a model of mutual repulsion

246 We replaced our calculation of cloud-based pulling forces with the mutual repulsion forces presented by Dutta and  
247 colleagues<sup>12</sup>, which was tuned on a later stage of *Drosophila melanogaster* development. With this model, there is a  
248 decay in nuclear speed as nuclei separate from one another (see Equation 2<sup>12</sup>, data not shown). This is the opposite  
249 of what we observe in real *G. bimaculatus* embryos and in simulations that use pulling clouds. In both cases, nuclei  
250 that move fastest are those that are farthest from other nuclei. Therefore, we concluded that a mechanism based on  
251 mutual repulsion does not effectively explain nucleus movements in *G. bimaculatus*.

## 252 5 Methods for physically constricting embryos

### 253 5.1 Assembling the embryo constriction device

254 We constricted embryos in a custom device, constructed as follows: We used a laser cutter to cut the components  
255 from sheets of acrylic (thickness = 1.59 mm, McMaster-Carr 8560K172; thickness = 3.18 mm, McMaster-Carr  
256 8560K257), and then assembled them with acrylic welding solution (IPS Weld-On 3 Acrylic Plastic Cement) fol-  
257 lowing the procedure described previously<sup>7</sup>. A DXF design file of the acrylic components is included as Supple-  
258 mentary File 3. The device's construction also required a common binder clip (width = 20 mm), two steel nails  
259 (diameter = 2 mm; length = 39 mm), and a rubber band (thickness = 1 mm). We were able to successfully con-  
260 strict embryos with versions of the device that were assembled with several different types of nails, rubber bands,  
261 and binder clips (data not shown). We used a human hair as the constricting fiber. It was held in place by being  
262 pinched in a block of elastomer (Dow Corning Sylgard 184 Elastomer Kit) into which a slit had been cut with a  
263 razor blade. We used a crafting hot glue gun to attach acrylic components to non-acrylic components. Schematics  
264 of all components are shown to scale along with additional assembly instructions in Fig. S1.

### 265 5.2 Using the embryo constriction device

266 Figure S2A is a photograph of the device in use, with human hairs used as the constricting fibers. We placed embryos  
267 in water-filled acrylic troughs on a removable platform, and then constricted them one at a time. To do so, we  
268 threaded a hair through the removable plastic platform, around an embryo, back through a hole at the bottom of  
269 a trough in the removable platform, and then attached it to a ratchet mechanism. Detailed instructions for this  
270 procedure are shown in Fig. S2B. This allowed us to increase tension on the hair while observing the embryo under  
271 a dissection microscope. As we increased tension, the embryo was incrementally constricted. After the desired  
272 extent of constriction was achieved, we placed temporary dabs of hot glue to affix the hair in place for the duration  
273 of imaging.

274 The device was able to hold multiple constricted embryos at a time for simultaneous imaging, up to a maximum  
275 of seven embryos. Once a set of embryos was constricted, we took the removable platform from the constriction  
276 device, placed it in a glass bottom 6-well dish (MatTek Po6G-1.5-20-F), and imaged it using a Zeiss Cell Discoverer  
277 microscope following previously described methods<sup>7</sup>.

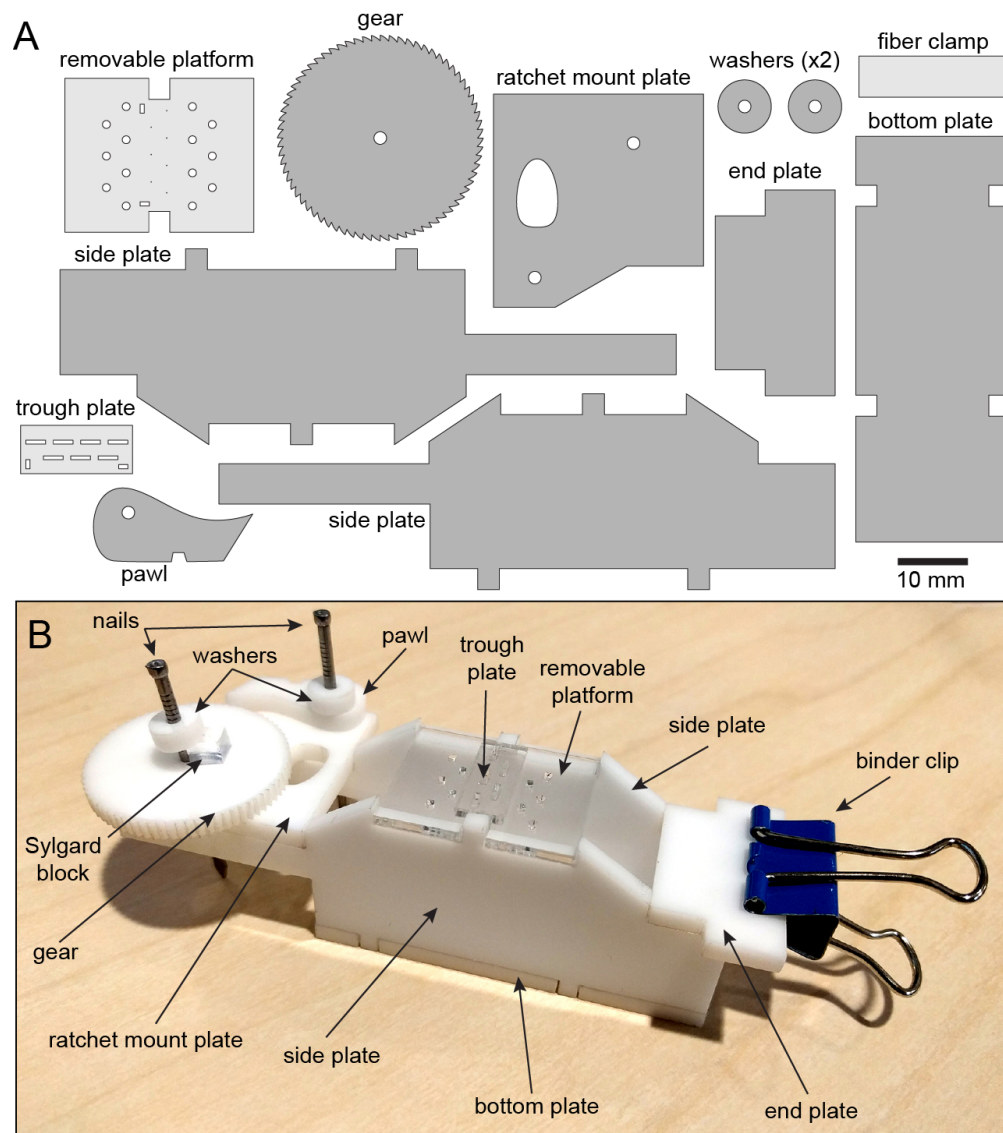


**Figure S1: Assembling a device for constricting embryos.** **A**, Diagram of all acrylic components. We cut the light gray pieces from 1.59 mm-thick acrylic sheet. We cut the rest from 3.18 mm-thick acrylic sheet. **B**, The assembled device also included a binder clip and two steel nails. Before welding the trough plate to the removable platform, we positioned trough plate so that the rectangular holes in the platform lined up with the corresponding holes in the trough plate. After the rest of the components were welded together as shown, we inserted one steel nail through a washer, then through the pawl, then through the ratchet mount plate. We applied hot glue to the top of the washer, fixing it to the nail. We also applied hot glue to the underside of the ratchet mount plate where the nail emerged, fixing the nail to the plate. We used a straight edge razor to cut a block of Sylgard elastomer with approximate dimensions 4 mm × 8 mm × 8 mm, and then sliced the block through half its depth when oriented with the largest face flat on a table. We inserted the second nail through the other washer, gear, and then the ratchet mount plate. We positioned the Sylgard block as shown, and then hot glued to the gear. We applied hot glue to the top of the second washer, fixing it to the nail. Finally, we applied more hot glue to the nail where it emerged underneath the ratchet mount plate, fixing it in place.

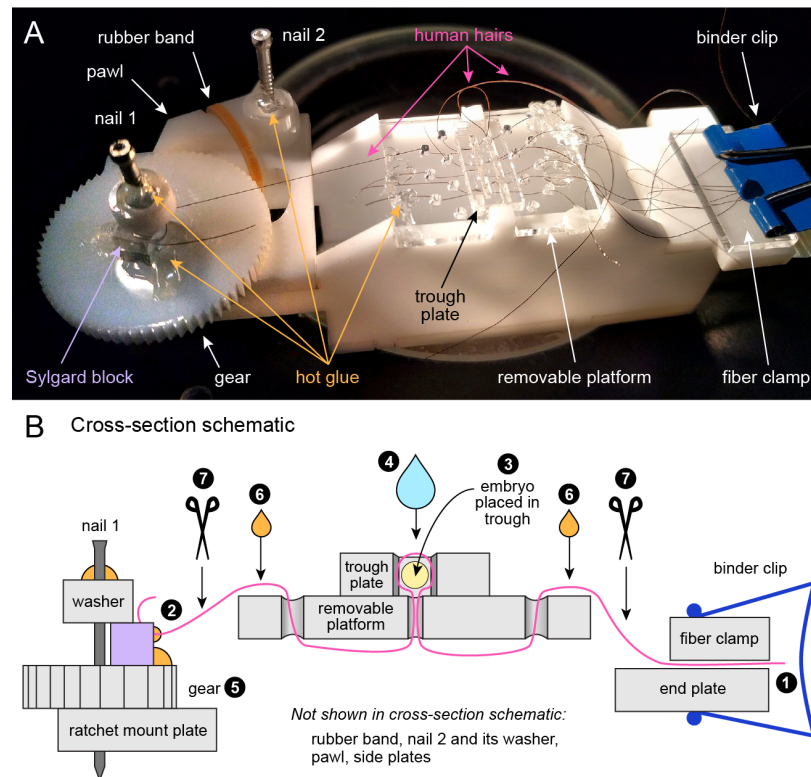


Figure S2: **Constricting embryos.** **A**, Photograph of the constriction device in use on a dissection microscope. To prepare the device for use, we cut a small rubber band to linearize it, inserted it through the largest hole in the ratchet mount plate, wrapped it underneath the side plate, and then rejoined it to itself by tying a knot. The re-joined rubber band formed a loop with the band slotting into the notch on the pawl, as shown. The tension on the rubber band pushed the pawl against the gear to make a ratchet. White arrows highlight the rubber band, binder clip, fiber clamp, removable platform, and gear. Hot glue is indicated with orange arrows. Note: the hot glue, rubber band, and fiber clamp were not shown in Fig. S1. The fiber clamp was an unattached rectangle of acrylic that, when squeezed by the binder clip, effectively held the fibers clamped in place. **B**, Cut-away schematic of fiber threading path (not to scale). Acrylic components are depicted in light gray, nail in dark gray, Sylgard block in lavender, hot glue in orange, water in light blue, and binder clip in dark blue. The embryo is shown in yellow as a cross-section end-on. The constricting fiber (a human hair) is shown in pink.

1. We clamped one hair between the end plate and fiber clamp.
2. We threaded the hair by hand through the path shown, and ultimately inserted into it the slit in the elastomer block, leaving a large loop in the place around the trough where the embryo would go. The removable platform can be taken off of the device to make threading easier.
3. We placed the embryo into the trough.
4. We added distilled water to the trough to fill its entire volume.
5. We manually cranked the gear while the embryo was observed by the user with a dissection microscope. Surface tension kept the water from leaking through the bottom hole.
6. When the desired constriction was achieved, we used hot glue to affix the hair at the two locations indicated with orange droplets.
7. We used scissors to cut the hair at the two locations indicated with the scissors icons. We repeated the constriction process on multiple embryos and then removed the removable plate. To image the embryos, we inverted the removable plate, with constricted embryos still in the troughs, and placed it into a coverslip-bottomed dish. We filled the dish with distilled water, and then imaged the embryos with an inverted microscope.

## 6 Code, data, and materials availability

A GitHub repository ([https://github.com/hoffmannjordan/gryllus\\_nuclear\\_movements](https://github.com/hoffmannjordan/gryllus_nuclear_movements)) has the code used to simulate nuclear movements during blastoderm formation and the code used to convert the tracking output from Ilastik into an XML file that was parsable by MaMuT. Plots were generated with Mathematica; notebooks used to generate each type of data visualization are available from the corresponding authors upon request.

A dataset of 3D+T nucleus positions and tracking links that supports the findings of this study is available at the GitHub repository for this project as well. Additional data that support the findings of this study are available from the corresponding authors upon reasonable request.

The *G. bimaculatus* culture is available for sharing from the corresponding authors upon request, provided that the requestor obtains the necessary permits for the transfer and continued maintenance of the culture (the specific permits will vary by jurisdiction). The plasmid for generating the Act-mtdT transgenic line described in the present study will likewise be available from the corresponding authors upon reasonable request.

## References

1. Preibisch, S., Saalfeld, S., Schindelin, J. & Tomancak, P. Software for bead-based registration of selective plane illumination microscopy data. *Nature Methods* **7**, 418–419 (2010).
2. Preibisch, S. *et al.* Efficient Bayesian-based multiview deconvolution. *Nature Methods* **11**, 645–648 (2014).
3. Schindelin, J. *et al.* Fiji: an open-source platform for biological-image analysis. *Nature Methods* **9**, 676–682 (2012).
4. Schindelin, J., Rueden, C. T., Hiner, M. C. & Eliceiri, K. W. The ImageJ ecosystem: An open platform for biomedical image analysis. *Molecular Reproduction and Development* **82**, 518–529 (2015).
5. Berg, S. *et al.* ilastik: Interactive machine learning for (bio) image analysis. *Nature Methods* **16**, 1226–1232 (2019).
6. Wolff, C. *et al.* Multi-view light-sheet imaging and tracking with the MaMuT software reveals the cell lineage of a direct developing arthropod limb. *eLife* **7** (2018).
7. Donoughe, S., Kim, C. & Extavour, C. G. High-throughput live-imaging of embryos in microwell arrays using a modular specimen mounting system. *Biology Open* **7**, bio031260 (2018).
8. Nakamura, T. *et al.* Imaging of transgenic cricket embryos reveals cell movements consistent with a syncytial patterning mechanism. *Current Biology* **20**, 1641–1647 (2010).
9. Donoughe, S. & Extavour, C. G. Embryonic development of the cricket *Gryllus bimaculatus*. *Developmental Biology* **411**, 140–156 (2016).
10. The scikit-fmm Team. in (2019). <https://github.com/scikit-fmm/scikit-fmm> (2020).
11. Sethian, J. A. *Level set methods and fast marching methods* tech. rep. (Cambridge University Press, 1999).
12. Dutta, S., Djabrayan, N. J.-V., Torquato, S., Shvartsman, S. Y. & Krajnc, M. Self-similar dynamics of nuclear packing in the early *Drosophila* embryo. *Biophysical Journal* **117**, 743–750 (2019).